

Observation of topologically protected compact edge states in flux-dressed graphene photonic lattices

Gabriel Cáceres-Aravena^{1†}, Milica Nedić^{2†}, Paloma Vildoso^{3†}, Goran Gligorić², Jovana Petrović², Rodrigo A. Vicencio³, Aleksandra Maluckov^{2*}

¹Institute of Physics, University of Rostock, Rostock, 18051, Germany.

²Vinča Institute of Nuclear Sciences, National Institute of the Republic of Serbia, University of Belgrade, P.O.B. 522, Belgrade, 11001, Serbia.

³Departamento de Física and Millenium Institute for Research in Optics—MIRO, Facultad de Ciencias Físicas y Matemáticas, Universidad de Chile, Santiago, 8370448, Chile.

*Corresponding author(s). E-mail(s): sandram@vin.bg.ac.rs;

Contributing authors: gabriel.caceres-aravena@uni-rostock.de;

milica.brankovic@vin.bg.ac.rs; palomavildoso1@gmail.com;

goran79@vin.bg.ac.rs; jovanap@vin.bg.ac.rs; rvcencio@uchile.cl;

†These authors contributed equally to this work.

Keywords: topological photonics, synthetic flux, photonic graphene, compact edge mode

Abstract

Systems with engineered flatband spectra are a postulate of high-capacity transmission links and a candidate for high-temperature superconductivity. However, their operation relies on the edge or surface modes susceptible to fluctuations and fabrication errors. While the mode robustness can be enhanced by a combination of Aharonov-Bohm caging and topological insulation, the design of the corresponding flatbands requires approaches beyond the standard k -vector-based methods. Here, we propose a synthetic-flux probe as a solution to this problem and a route to the realization of

ultra-stable modes. We prove the concept in a laser-fabricated graphene-like ribbon photonic lattice with the band-flattening flux induced by “P” waveguide coupling. The topological non-triviality is witnessed by an integer Zak phase derived from the mean chiral displacement. Mode stability is evidenced by excellent mode localization and the robustness to fabrication tolerances and variations of the input phase. Our results can serve as a basis for the development of multi-flat-band materials for low-energy electronics.

1 INTRODUCTION

The quest for materials with superconducting properties at convenient operating temperatures has gained new momentum with the possibility to investigate such materials in affordable optics experiments, notably in photonic lattices [1–5]. Departing from the traditional Bardeen–Cooper–Schrieffer (BCS) theory, it has been hypothesized that the electron pairing around dispersionless energy bands results in superconductivity with the critical temperature linearly proportional to the electron interaction strength[6]. However, dispersionless bands, commonly known as flat bands (FBs), store energy in the modes confined to edges, surfaces or interfaces. This makes them highly sensitive to environmental influences and fabrication errors [7–9]. Stability can be enhanced by topological insulation achieved by an interplay between the Aharonov–Bohm caging and topological protection, such as that realized in Creutz-like ladders [10–12]. However, k -independence of FBs does not permit determination of the topological invariants, neither directly, based on the Berry-curvature, nor indirectly, based on analogy with the Su–Schrieffer–Heeger (SSH) model [13, 14]. Exceptions are the configurations which allow Hamiltonian reduction to the SSH Hamiltonians [10]. All this makes the design of ultra-robust edge states with the FB spectrum difficult.

In response to these challenges, we design a graphene-like photonic ribbon whose topological properties can be controlled by synthetic flux. The all FB ribbon spectrum is achieved for π -flux, which is realized by inserting only S or S and P waveguides in a particular order through the lattice, [15]. The induced transitions between trivial and nontrivial topological phases enable probing of the dispersionless band topology and determination of the topological invariants. Topological transitions are detectable by standard means: two-band SSH-based graphical method, mean chiral displacement (MCD) [16–18] and numerical projector method [14, 19, 20]. While a range of fluxes drives the system into the topologically nontrivial phase, a particular flux value, $\Phi = \pi$, yields destructive interference and ultimate band-flattening. The corresponding edge modes are ultra-protected by the synergy of Aharonov–Bohm (AB) and topological effects.

For verification of the proposed flux method, we use the femtosecond (fs) laser writing technique [21] to inscribe a lattice in the form of a quasi-1D graphene ribbon in armchair configuration [22, 23]. By determining the MCD from the experimental data, we confirm the topological nontriviality of the central bands and the corresponding edge modes. We demonstrate a zero-mode edge state and its robustness to the input-state phase variations and fabrication tolerances. To the best of our knowledge, this

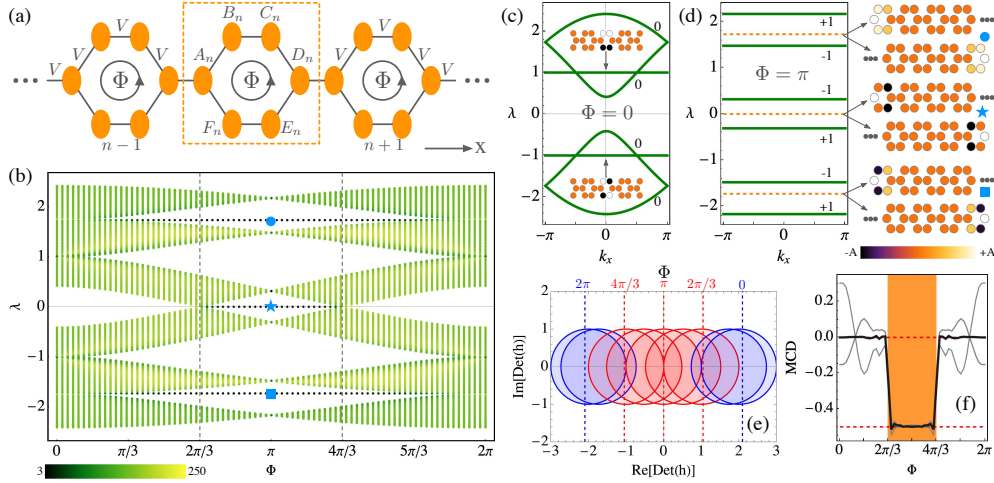


Fig. 1 (a) Schematic graphene-like ribbon lattice including a flux Φ on every hexagonal ring. (b) Energy-band spectrum of a finite lattice ($N = 50$ unit cells) as a function of flux Φ . The topologically non-trivial domain $\Phi \in [2\pi/3, 4\pi/3]$ is bounded by vertical dashed lines. (c) and (d) show the band spectra λ vs. k_x , inside the 1st Brillouin zone (BZ), for fluxes $\Phi = 0$ and $\Phi = \pi$, respectively. In (d) the edge-states correspond to horizontal dashed lines, with the respective mode profiles to the right. Energy spectra are normalized by $V = 1$. (e) Determinant $\text{Det}(h) = -\cos k_x + 2\cos(\Phi/2) + i\sin k_x$, of SSH-like reduced Hamiltonian h , in the complex plain (see Supplementary Information). The red circles wind around or touch the origin, defining the nontrivial topological cases. (f) The mean chiral displacement (MCD) as a function of Φ (black solid line). Gray lines correspond to the mean field displacements from initially excited single A, C, E sites (Supplement).

is the first complete experimental evidence of an ultra-robust and perfectly compact topologically nontrivial edge state in a one-dimensional lattice.

2 RESULTS

Topological invariants and lattice properties

We first present the method for probing the topological triviality of a lattice by artificial flux. We do this on a model of a hexagonal graphene-like ribbon in the armchair configuration. In the absence of flux, the underlying lattice structure is characterized by bipartite and top-bottom symmetries, in which each unit cell consists of six linearly coupled sites, as described in Figure 1(a). Evolution of the complex optical field $\psi_n = (A_n \ B_n \ C_n \ D_n \ E_n \ F_n)^T$, with $n = 1, \dots, N$ and N the number of unit cells, is governed by a set of linear coupled equations in k_x -space:

$$i \frac{d\tilde{\psi}(k_x)}{dz} = H(k_x)\tilde{\psi}(k_x), \quad (1)$$

where $\tilde{\psi}(k_x)$ is the optical field in k_x -space, k_x the transversal quasimomentum, z the propagation coordinate, and H the Bloch Hamiltonian or lattice coupling matrix. The

presence of flux Φ breaks the symmetry and introduces imaginary components into the coupling coefficients:

$$\hat{H} = V \begin{pmatrix} 0 & e^{-i\phi} & 0 & e^{-ik_x} & 0 & e^{i\phi} \\ e^{i\phi} & 0 & e^{-i\phi} & 0 & 0 & 0 \\ 0 & e^{i\phi} & 0 & e^{-i\phi} & 0 & 0 \\ e^{ik_x} & 0 & e^{i\phi} & 0 & e^{-i\phi} & 0 \\ 0 & 0 & 0 & e^{i\phi} & 0 & e^{-i\phi} \\ e^{-i\phi} & 0 & 0 & 0 & e^{i\phi} & 0 \end{pmatrix}, \quad (2)$$

where $\phi = \Phi/6$. $Ve^{\pm i\phi}$ are the complex intra-cell coupling coefficients, while $Ve^{\pm ik_x}$ are the inter-cell coupling coefficients (for simplicity, we have set the unit cell distance as 1), according to the geometry described in Fig. 1(a) (more details on equations at Supplementary material).

We compute the eigenvalue spectrum $\{\lambda\}$ representing the longitudinal propagation constants along the z direction for a finite lattice with $N = 50$ unit cells, and show our results in Fig. 1(b), where darker color corresponds to a smaller participation ratio, i.e. stronger localization. In the absence of flux [see Fig. 1(c)], the bipartite ribbon spectrum contains an empty gap around zero, a pair of symmetric flat bands at $\lambda = \pm V$ (with the FB states as insets), and two pairs of dispersive bands [15]. In this case, there are no isolated bands, and the topological invariant is not defined. The introduction of flux breaks the top-bottom ribbon symmetry, whereas the chiral symmetry is preserved. Singular FBs are transformed into gapped dispersive bands and an opening of the gaps between outer bands appears. The two outer gaps host a doublet of edge modes each [circle and square in Figs. 1(b) and (d)]. A further increment in flux Φ results in the closing and reopening of the central gap at $\Phi = 2\pi/3$ - followed by the creation of a pair of zero ($\lambda = 0$) edge modes [star in Fig. 1(b)], in analogy with the SSH system [24]. These degenerated edge modes decay exponentially from the respective surface and their localization increases as the central band gap increases (see Supplementary information). The spectrum symmetry dictates the reverse trend as the flux is further increased, closing the gap at $\Phi = 4\pi/3$ and restoring the original trivial properties.

For a particular value of flux $\Phi = \pi$, the Aharonov-Bohm effect causes the bands to collapse into flat bands [25], forming a fully flat multi-band spectrum, as Figs. 1(b) and (d) clearly show. The flatness is associated with degeneration of $6(N - 1)$ eigenvalues into 6 flat bands at $\lambda = \pm 2.17V, \pm 1.48V, \pm 0.31V$ with $N - 1$ -times degeneration each. In the gaps, in between the flat bands, the triplet of double degenerated edge modes continues to exist at $\lambda = 0, \pm \sqrt{3}V$ [horizontal dashed lines and respective edge mode profiles in Fig. 1(d)]. As the result of destructive interference, all the corresponding edge mode profiles feature zero light power at the connecting lattice sites A or D. This fully prevents state transport and dispersion. Specifically, at $\Phi = \pi$, the zero edge modes are perfectly compact and formed by only three nonzero amplitude sites. These perfectly compact edge states cannot be formed by any FB states superposition [26].

An estimate of bulk topological invariant is mandatory to ascertain the topological non-triviality of the compact edge states. However, the topological invariants elude a clear definition in the systems with FB k -independent spectrum. To resolve this,

we tune the synthetic flux and evaluate the invariant (Zak phase in this case), in the k -dependent spectral region, upon which we formally converge to values at $\Phi = \pi$. Zak phase, also known as winding number (Supplementary information), provides information about the winding behavior of the energy bands in the momentum space, distinguishing between different topological phases in the lattice. Due to the bulk-edge correspondence [27–29], an integer value of Zak phase in units of π is equal to the number of edge-mode pairs within a gap and signals topological non-triviality. Here, we evaluate the Zak phase by two methods: the geometric method developed on the SSH-analogy [14] and the mean chiral displacement method [16–18] (results are corroborated by projector method in Supplementary information).

Re-opening and re-closing of the central gap, accompanied by the appearance of the zero edge modes, is analogous to what is observed in the SSH model. This is corroborated by the transformation of Hamiltonian of the flux-dressed ribbon lattice into an SSH Hamiltonian parameterized by flux, as shown in Supplementary information. The winding number of the SSH Hamiltonian can be estimated by plotting its determinant in the complex plane and observing how many times it winds around the origin, see Fig. 1(e). The topological phase transition is marked by the zeros of the determinant at $\Phi = 2\pi/3$ and $\Phi = 4\pi/3$. The flux values within these limits render the lattice topologically non-trivial regime. For $\Phi = \pi$, the determinant draws a zero-centred circle, thus reproducing the k_x -invariance.

The non-triviality of the zero edge mode is further confirmed by the MCD calculated as a displacement (in cells units) of the spatial profile from the input position [16],[30],[31]. It has been shown that in a lattice with 2 FBs, MCD value close to 1/2 signals the non-trivial topological phase [30–32]. In Fig. 1(f), we plot the dependence of MCD with respect to flux Φ and observe that the MCD takes values close to -1/2 in the whole non-trivial region $\Phi \in [2\pi/3, 4\pi/3]$. This result indicates that the MCD can be used as a nontriviality parameter also in a lattice with multiple FBs. Final confirmation of the zero-edge mode topological nontriviality is achieved by applying the projector method, as described in Supplementary information.

Based on the above, we conclude that the zero edge modes are protected by both the destructive interference (arising from Aharonov-Bohm caging) and the lattice topology. Hence, these states are perfectly localized, compact, and ultra-stable stationary solutions. Their chiral symmetry remains intact during the topological to trivial transitions.

Experiments on flux-dressed graphene photonic lattices

We provide evidence of the trivial and topological properties of a graphene-like ribbon lattice in two experimentally available fluxes cases: $\Phi = 0, \pi$. Different graphene-like photonic lattices are fabricated inside a $L = 70$ mm borosilicate glass by direct laser writing [21], as sketched in Fig. 2(a). If the lattice is composed of S identical waveguides only, no flux ($\Phi = 0$) is induced. Fig. 2(b1) shows a sketch for a trivial S lattice and Fig. 2(c1) its implementation. A nontrivial flux is induced by replacing a set of S waveguides with dipole-like P waveguides at every other hexagon, as described in Figs. 2(b2) and (c2). The presence of P waveguides on a lattice produces the appearance of negative coupling constants and, therefore, an effective induction

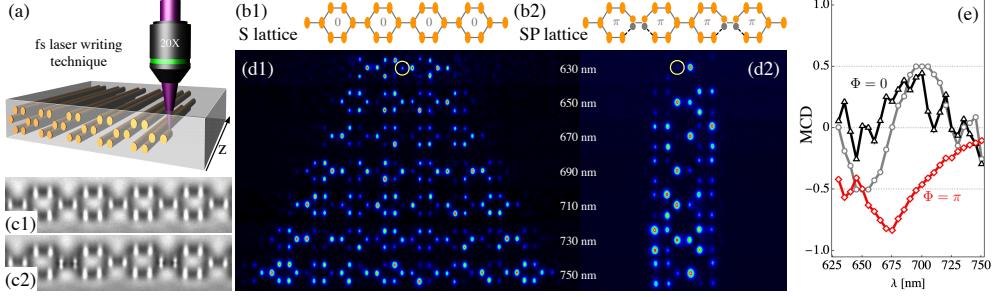


Fig. 2 Bulk excitation. (a) Illustration of the fs-laser writing technique for a graphene-like ribbon. (b1) and (b2) show S and SP configurations (fluxes denoted in each case). (c1) and (c2) show white-light microscope images for the fabricated lattices. (d1) and (d2) present output intensities after single site excitations (at sites indicated by yellow circles), on a ribbon with $\Phi = 0$ and $\Phi = \pi$, respectively. The input wavelength is indicated at the center. (e) Mean chiral displacement for sites ACE versus wavelength, for trivial (black) and topological (red) lattices. Gray data in (e) shows the average MCD for CE sites only.

of flux $\Phi = \pi$ on closed rings [25]. Effective interaction in between S and P modes is controlled by a tuning optimization protocol [33], which matches the propagation constants of different modes at a given wavelength. Here, the required flux $\Phi = \pi$ is optimized at a wavelength 640 nm.

To study the light transport through the lattices, we exploit the monotonous dependence of the coupling length on wavelength [31]. We capture the transport at different dynamical instants in a lattice of a fixed length, L , by simply varying the input wavelength (see Methods for more details). These experiments were performed using a supercontinuum (SC) laser source, in the wavelength range of $\{630, 750\}$ nm, focused to excite an individual lattice site in the middle (bulk excitation) or at the edge of the lattice (edge excitation).

We first excite the trivial lattice at the bulk D site [Fig. 2(d1)] and observe a ballistic transport across the lattice, similar to 1D discrete diffraction [31]. In this case, the input excitation does not excite the FB modes. Therefore, only the dispersive part of the spectrum is activated. Inclusion of the FB along with the dispersive modes, e.g., by excitation of B, C, D, E sites, results in a mixture of diffraction and energy oscillations strongly localized at the input ring region [15] (graphs in Supplementary information). A strongly contrasting behaviour is observed for a nontrivial flux $\Phi = \pi$, as shown in Fig. 2(d2). For an identical bulk D excitation, the light cannot overcome the flux-induced effective barrier and remains oscillating on a reduced area, covering only two lattice rings. This is a result of the AB caging effect in a system with a flat-only linear spectrum [Fig. 1(d)].

For bulk excitation, we compute the MCD from the experimental results by averaging the excitation of A, C and E bulk lattice sites [see Fig. 2(e)], consistently with the lattice chiral symmetry (see Methods). For $\Phi = 0$, the MCD oscillates around zero, indicating a zero Zak phase. In this case, the light is diffracting strongly through the lattice [Fig. 2(d1)] and experiencing different inhomogeneities induced by the fabrication process, which randomizes the MCD value. The average of CE sites only [grey

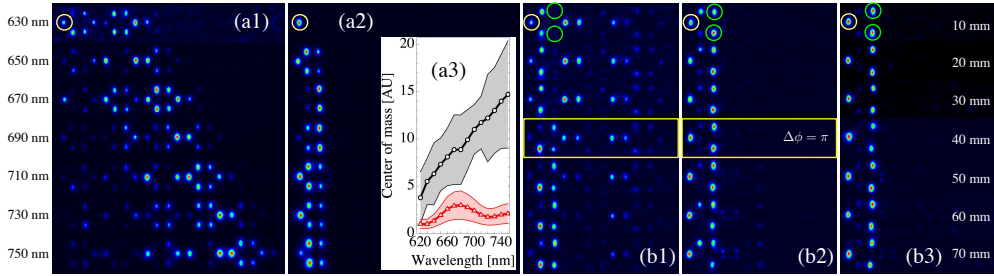


Fig. 3 (a) Edge *A* site excitation: (a1) and (a2) output intensities for the excitation of S and SP lattices, respectively, and for the wavelengths indicated to the left. (a3) Center of mass versus wavelength for the S (black) and SP (red) lattices, with the shaded area showing the second moment. (b) SLM edge excitation: (b1) and (b2) sweep of the relative input phase $\Delta\phi$ in between site *A* (yellow) and sites *C, E* (green). Vertical images show different input phases around $\Delta\phi = \pi$ (yellow frame). (b3) Excitation of the edge compact topological state at $\Delta\phi = \pi$ versus the propagation distance z_s indicated to the right.

data in Fig. 2(e)] shows an oscillation around zero, as these two sites support mainly the FBs that bound the light on a single unit cell. For $\Phi = \pi$, the nontriviality of the lattice becomes evident with MCD values around -0.5 . Indeed, the MCD is closest to -0.5 around the wavelength of 640 nm, for which the nontriviality condition is fully fulfilled. It is proportional to an integer value of Zak-phase $Z_p[\pi] = 2MCD = \pm 1$. Therefore, we have experimentally demonstrated the trivial and nontrivial properties of the graphene-like ribbon and showed directly the bulk-boundary correspondence for the topologically compact edge states.

To study the edge excitation, we first excite the site *A* at the left edge of both lattices. In the trivial $\Phi = 0$ lattice, we observe only transport with the light strongly repelled from the edge; see Fig. 3(a1). It is a direct consequence of the absence of edge states from the spectrum shown in Fig. 1(c). In the presence of nontrivial flux, we observe a remarkable effect. The light remains trapped to the first unit cell, oscillating locally due to the simultaneous excitation of three edge modes. In Fig. 3(a2), a revival is observed around 720 nm. To compare the light propagation through these lattices, we plot the centre of mass as a function of wavelength, with a shaded area showing the second moment as an indicator of the profile width. We observe that, in the trivial lattice (black data), the light escapes away from the edge and strongly disperses. In the topological system (red data), the light oscillates within the first cell with almost no dispersion, confirming the observed revival. While the tuning condition was optimized in the fabrication around 640 nm, the results show that the destructive interference condition at $\Phi = \pi$ is valid beyond the tuning zero regime. Nevertheless, we stop measuring at 750 nm to avoid next-nearest-neighbour coupling effects.

We further investigate the robustness of the compact zero-edge modes. An image generator simultaneously excites different lattice sites with a given phase structure. We generate a three-site input state at 640 nm and excite sites *A, C* and *E* at the left edge. As shown by yellow and green circles in Fig. 3(b), *C* and *E* are excited in phase, while the excitation phase in *A* is varied with a relative phase difference around $\Delta\phi = \pi$. The results for trivial lattice in Fig. 3(b1) show clear signatures of dispersion

and FB oscillations without a tendency for edge localization. On the other hand, for $\Phi = \pi$ [see Fig. 3(b2)], we observe that the light gets trapped at the first unit cell with almost no dispersion to the lattice bulk. The localization persists regardless of the phase structure of the input light, thus showing the robustness of the compact edge modes to input phase deviations. This is particularly important in applications in which the phase of an excitation beam is subject to fluctuations.

Finally, we study the compact-edge-mode propagation stability and robustness to fabrication tolerances. We fix the input phase to $\Delta\phi = \pi$ and fabricate a z-scan configuration [25], in which the excited sites A , C and E , at the first unit cell only, have the maximum length allowed by the substrate (70 mm), while the rest of the lattice sites have a shorter z_s length. To follow the state evolution along the lattice, we fabricate 14 lattices with different z_s and show a selected set of output profiles in Fig. 3(b3). We observe an excellent stability of the compact edge mode along propagation. As each lattice is fabricated independently of the others, a random fabrication disorder is present in every sample, which allows us to conclude that the zero-edge mode is resistant to the small variations in the lattice structure. This result is also confirmed numerically by a deliberate introduction of disorder into the Hamiltonian (2) (Supplementary information).

3 DISCUSSION

The main achievements of the presented study are the generation of highly robust topologically protected compact edge modes and the establishment of a novel procedure for the assessment of topological nontriviality via the mean chiral displacement. Demonstration of the stable compact edge modes is a decisive stepping stone towards unidirectional topological insulators. Further upgrades, including the non-Hermitian Hamiltonian to achieve unidirectional mode propagation and the inclusion of higher dimensions, will make the topological photonic lattices a faithful model for ultra-low energy electronics or photonics computing. The experimental implementation of synthetic flux and the corresponding MCD estimation open the door to the detection of topological nontriviality in multiband dispersionless systems.

4 METHODS

The mean chirality displacement

The MCD is used to determine the Zak phase in 1D multi-band bipartite lattices with inherent chiral symmetry and isolated bands [16–18]. It is an extension of the mean field displacement (MFD) method widely used in 1D two-band systems [30–32], which is based on the geometric (Berry) phase. The geometric phase is proportional to the displacement of the centre of mass of Wannier functions, which form the basis complementary to the Bloch basis [19].

In the literature, the MFD is determined numerically and experimentally by the mean displacement of the centre of propagating wavepacket initiated by single site lattice excitation [30–32]:

$$M_{FD}(L_z) = \frac{1}{L_z} \int_{z=0}^{z=L_z} \frac{\sum_{n=0}^{N-1} (x_n(z) - x_n(0)) |\psi_n(z)|^2}{\sum_{n=0}^{N-1} |\psi_n(z)|^2} dz, \quad (3)$$

where L_z is the propagation distance in the z -axis direction and x is position in ribbon, and $\Psi = [\psi_1 \psi_2 \dots \psi_N]^T$ is the wavepacket.

In our numerical calculations and experiments, we excite the sites of the central unit cell hosting an eigenstate of the chiral operator, i.e., A , C , and E for the state with the eigenvalue 1 or B , D , and F for the state with the eigenvalue -1 . The sites are excited one by one and the MCF is determined as an average value of the three displacements.

Finally, the Zak phase is obtained as a twofold value of the mean chiral displacement $Z_p[\pi] = 2M_{CD}$ and, according to the bulk-edge correspondence, equals the number of topologically protected edge modes [28, 29].

The details of the calculation and chirality model are presented in Supplementary information.

Lattice fabrication and characterisation

The lattices were fabricated by direct laser writing technique [21] sketched in Fig. 2(a). A femtosecond laser of 1030 nm was tightly focused onto a borosilicate glass wafer, which was translated along z to inscribe the waveguides and in $x - y$ plane to achieve the designed lattice profile. The synthetic flux was induced by replacing some S lattice sites with dipole-like P waveguides, as shown in Fig. 2(c1) and (c2), and optimizing the interaction between them by a wavelength tuning scheme [25, 33]. The zero-detuning condition was achieved at 640 nm, but the flux $\Phi = \pi$ was obtained for a much broader wavelength range as demonstrated in the experiments.

The characterization experiments were performed by a horizontally polarized supercontinuum (SC) laser source in the wavelength range of {630, 750} nm. When the excitation wavelength is increased, the guided-mode width increases and, therefore, the coupling constant becomes larger [31], effectively increasing the propagation length. Hence, by varying the input wavelength, we can study a system with a fixed glass length, L , but at a different dynamical instant.

The edge mode profile was excited by an amplitude- and phase-modulated beam obtained from an image generator setup (see Supplementary information for details). The beam was first amplitude-modulated by a Holoeye LC2012 transmission spatial light modulator (SLM) to enable simultaneous excitation of multiple waveguides. Subsequently, the phase was modulated by a Holoeye PLUTO reflection SLM. The final image is transferred to the input facet of the photonic chip by a telescope and a $4\times$

microscope objective. The array output is imaged using a $10\times$ objective and recorded by a CCD camera.

Declarations

Data availability. All data needed to evaluate the conclusions in the paper are available in this Article or its Supplementary Information. The data that support the findings of this study are available from the corresponding authors upon reasonable request.

Acknowledgments. This research was supported in part by Ministry of Science, Technological Development and Innovation of the Republic of Serbia (451-03-9/2021-14/ 200017), Millennium Science Initiative Program ICN17_012, FONDECYT Grant 1231313, and the IRTG “Imaging Quantum Systems” No. 437567992 by the German Research Foundation.

Author contributions. G.C.-A. performed analytical calculations; M.N. and G.G. designed numerical model; G.C.-A., M.N., and G.G. performed numerical simulations; P.V. and R.V. designed and performed the experiments; G.G., J.P., R.A.V. and A.M. analyzed results and performed checking of results; R.A.V. and A. M. initialized and supervised the project. All the authors contributed to the final form of the manuscript.

Competing interests. The authors declare no competing interests.

Additional information.

Supplementary information. The online version contains supplementary material available at ...

Correspondence and requests for materials. Address to R.A. Vicencio and A. Maluckov

References

- [1] Mandal, M., Drucker, N., C., Siriviboon, P., Nguyen, T., Boonkird, A., Lamichhane, T. N., Okabe, R., Chotrattanapituk, A. & Li, M. Topological Superconductors from a Materials Perspective. *Chem. Mater.* **35**, 16, 6184–6200 (2023).
- [2] Liu, G., Lu, S., Gao, Y., Wang, F., Jia, B., Guan, X., Han, L. H., Lu, P. & Song, H. Band structure optimization of superconducting photonic crystals based on transmission spectrum calculation. *Opt. Express* **31**, 41905-41918 (2023).
- [3] Ozawa, T., El-Ganainy, R. & Amo, A. Photonic Topological Materials: feature introduction. *Opt. Mater. Express* **11**, 1592-1593 (2021).
- [4] Khanikaev, A., Hossein Mousavi, S., Tse, WK., Kargarian, M., MacDonald A. H. & Shvets G. Photonic topological insulators. *Nature Mater.* **12**, 233–239 (2013).

- [5] Price H. et al. Roadmap on topological photonics. *J. Phys. Photonics* **4**, 032501 (2022).
- [6] Heikkilä, T. T. & Volovik, G. E. Flat bands as a route to high-temperature superconductivity in graphite. In *Basic Physics of Functionalized Graphite. Springer Series in Materials Science* (eds. Esquinazi, P.) 123-143 (Springer, Cham. 2016)
- [7] Tovmasyan M, Peotta S, Törmä P & Huber, S. D. Effective theory and emergent SU(2) symmetry in the flat bands of attractive Hubbard models, external page *Phys. Rev. B* **94**, 245149 (2016)
- [8] Hofmann, J. S., Assaad, F. F. & Schnyder, A. P. Edge instabilities of topological superconductors. *Phys. Rev. B* **93**, 201116(R) (2016).
- [9] Tovmasyan, M., Peotta, S., Liang, L., Törmä, P. & Huber, S. D., Preformed pairs in flat Bloch bands, *Phys. Rev. B* **98**, 134513 (2018)
- [10] Zurita, J., Creffield, C. & Platero, G. Tunable zero modes and quantum interferences in flat-band topological insulators. *Quantum* **5**, 591 (2021).
- [11] Zurita, J., Creffield, C. & Platero, G. Topology and interactions in the photonic Creutz and Creutz-Hubbard ladders. *Adv. Quantum Technol.* **3**, 1900105 (2020).
- [12] Cáceres-Aravena, G. & Foa Torres, L. E. F. & Vicencio, R. A. Topological and flat-band states induced by hybridized linear interactions in one-dimensional photonic lattices. *Phys. Rev. A* **102**, 023505 (2020).
- [13] Lee, C.-S., Io, I.-F. & Kao, H.-C. Winding number and Zak phase in multi-band SSH models. *Chinese Journal of Physics* **78**, 96-110 (2022).
- [14] Asbóth J. K., Oroszlány, L. & Pályi, A. *A Short Course on Topological Insulators*. (Springer, Berlin, 2016).
- [15] Cantillano, C. et al. Observation of localized ground and excited orbitals in graphene photonic ribbons. *New J. Phys.* **20**, 033028 (2018).
- [16] Cardano, F. et al. Detection of Zak phases and topological invariants in a chiral quantum walk of twisted photons. *Nat. Comm.* **8**, 15516 (2017).
- [17] Maffei, M., Dauphin, A., Cardano, F., Lewenstein, M. & Massignan, P. Topological characterization of chiral models through their long time dynamics. *New J. Phys.* **20**, 013023 (2018).
- [18] D'Errico, A. et al. Bulk detection of time-dependent topological transitions in quenched chiral models. *Phys. Rev. Research* **2**, 023119 (2020).
- [19] Vanderbilt, D. *Berry Phases in Electronic Structure Theory: Electric Polarization, Orbital Magnetization and Topological Insulators*. (Cambridge: Cambridge

- University Press, 2018).
- [20] Leykam, D. & Smirnova, D. A. Probing bulk topological invariants using leaky photonic lattices. *Nat. Phys.* **17**, 632–638 (2021).
 - [21] Szameit, A. et al. Discrete nonlinear localization in femtosecond laser written waveguides in fused silica. *Opt. Express* **13**, 10552–10557 (2005).
 - [22] Jürß, C. & Bauer, D. High-order harmonic generation in hexagonal nanoribbons. *The European Physical Journal Special Topics* **230**, 4081–4089 (2021).
 - [23] Drüeke, H. & Bauerb, D. High-harmonic spectra of hexagonal nanoribbons from real-space time-dependent Schrödinger calculations. *The European Physical Journal Special Topics* **230**, 4065–4070 (2021).
 - [24] Delplace, P., Ullmo, D. & Montambaux, G. Zak phase and the existence of edge states in graphene. *Phys. Rev. B* **84**, 195452 (2011).
 - [25] Cáceres-Aravena, G., Guzmán-Silva, D., Salinas, I. & Vicencio, R. A. Controlled transport based on multiorbital Aharonov-Bohm photonic caging. *Phys. Rev. Lett.* **128**, 256602 (2022).
 - [26] Vicencio, R. A. Photonic flat band dynamics. *Adv. Phys.* **6**, 1878057 (2021).
 - [27] Leykam, D. & Smirnova, D. A. Photonic quantum Hall effect. In *Encyclopedia of Condensed Matter Physics (Second Edition)* (eds. Chakraborty, T.) 575-586 (Academic Press, 2024).
 - [28] Lu, L., Joannopoulos, J. D. & Soljačić, M. Topological photonics. *Nat. Photon.* **8**, 821 (2014).
 - [29] Ozawa, T. et al. Topological photonics. *Rev. Mod. Phys.* **91**, 015006 (2019).
 - [30] Jiao, Z.-Q., Longhi, S., Wang, X.-W., Gao, J., Zhou, W.-H., Wang, Y., Fu, Y.-X., Wang, L., Ren, R.-J., Qiao, L.-F. & Jin, X.-M. Experimentally detecting quantized Zak phases without chiral symmetry in photonic lattices. *Phys. Rev. Lett.* **127**, 147401 (2021).
 - [31] Cáceres-Aravena, G. et al. Edge-to-edge topological spectral transfer in diamond photonic lattices. *APL Photonics* **8**, 080801 (2023).
 - [32] Longhi, S. Probing one-dimensional topological phases in waveguide lattices with broken chiral symmetry, *Opt. Lett.* **43**, 4639–4642 (2018).
 - [33] Guzmán-Silva, D., Cáceres-Aravena, G. & Vicencio, R. A. Experimental observation of inter-orbital coupling. *Phys. Rev. Lett.* **127**, 066601 (2021).